Polarization transfer measurement for $^1\mathrm{H}(\vec{d},\vec{p})^2\mathrm{H}$ elastic scattering at 135 MeV/nucleon and three-nucleon force effects

K. Sekiguchi,[1,*] H. Sakai,[1,2,3] H. Witała,[4] K. Ermisch,[5] W. Glöckle,[6] J. Golak,[4] M. Hatano,[2] H. Kamada,[7] N. Kalantar-Nayestanaki,[5] H. Kato,[2] Y. Maeda,[2] J. Nishikawa,[8] A. Nogga,[9] T. Ohnishi,[1] H. Okamura,[10] T. Saito,[2] N. Sakamoto,[1] S. Sakoda,[2] Y. Satou,[11] K. Suda,[8] A. Tamii,[12] T. Uchigashima,[2] T. Uesaka,[3] T. Wakasa,[13] and K. Yako[2]

[1]*RIKEN, the Institute of Physical and Chemical Research, Wako, Saitama 351-0198, Japan*
[2]*Department of Physics, University of Tokyo, Bunkyo, Tokyo 113-0033, Japan*
[3]*Center for Nuclear Study, University of Tokyo, Bunkyo, Tokyo 113-0033, Japan*
[4]*Institute of Physics, Jagiellonian University, PL-30059 Cracow, Poland*
[5]*Kernfysisch Versneller Instituut, Zernikelaan 25, 9747 AA Groningen, The Netherlands*
[6]*Institut für theoretische Physik II, Ruhr-Universität Bochum, D-44780 Bochum, Germany*
[7]*Department of Physics, Faculty of Engineering, Kyushu Institute of Technology, Kitakyushu 804-8550, Japan*
[8]*Department of Physics, Saitama University, Saitama 338-8570, Japan*
[9]*Institute for Nuclear Theory, University of Washington, Seattle, Washington 98195-1550, USA*
[10]*Cyclotron and Radioisotope Center, Tohoku University, Sendai, Miyagi 980-8578, Japan*
[11]*Department of Physics, Tokyo Institute of Technology Meguro, Tokyo 152-8551, Japan*
[12]*Research Center for Nuclear Physics, Osaka University, Ibaraki, Osaka 567-0047, Japan*
[13]*Department of Physics, Kyushu University, Fukuoka 812-8581, Japan*

The deuteron-to-proton polarization-transfer coefficients for d-p elastic scattering were precisely measured with an incoming deuteron energy of 135 MeV/nucleon at the RIKEN Accelerator Research Facility. The data are compared to theoretical predictions based on exact solutions of the three-nucleon Faddeev equations with high-precision nucleon-nucleon forces combined with the current, most popular three-nucleon force (3NF) models: the 2π-exchange Tucson-Melbourne model, a modification thereof based on chiral symmetry, TM′(99), and the Urbana IX 3NF. Theory predicts large 3NF effects, especially in the angular range around the cross section minimum, predominantly for $K_{xx}^{y'}-K_{yy}^{y'}$ $(K_{xx}^{y'},K_{yy}^{y'})$, but the present data only partially concurs with the calculations. For the induced polarization, $P^{y'}$, the TM′(99) and Urbana IX 3NFs reproduce the data, but the Tucson-Melbourne 3NF fails to describe the data. For the polarization-transfer coefficients, $K_y^{y'}$ and $K_{xz}^{y'}$, the predicted 3NF effects are in drastic disagreement with the data. These facts clearly reveal the defects of the 3NF models currently used.

I. INTRODUCTION

A main interest of nuclear physics is to understand the forces acting between nuclear constituents. Few-nucleon systems offer unique opportunities to investigate these forces. Intensive theoretical and experimental efforts have established high-precision nucleon-nucleon (*NN*) potentials, partly based on one-meson exchange, partly on phenomenology, namely AV18 [1], CDBonn [2–4], Nijmegen I, II and 93 [5]. They reproduce a rich set of experimental *NN* data up to a laboratory energy of 350 MeV with very high precision, expressed in terms of χ^2 per data points of very close to one. However, these so-called realistic *NN* forces fail to predict the correct experimental binding energies of few-nucleon systems, resulting in a clear underbinding. For three- and four-nucleon systems, where exact solutions of the Schrödinger equation are available for these interactions, this underbinding amounts to 0.5–1 MeV in case of ^{3}H and ^{3}He, and to 2–4 MeV for ^{4}He [6]. Also, for higher mass nuclei up to $A=10$, where stochastic techniques have been applied, realistic *NN* forces fail to provide the measured binding energies [7,8], which is generally seen as the first indication of missing three-nucleon forces (3NFs) in the nuclear Hamiltonian. Presently, the common 3NF models are based on the 2π-exchange between three nucleons, and the main ingredient is the Δ-isobar excitation, initially proposed by Fujita and Miyazawa almost half a century ago [9]. Further improvements have led to the Tucson-Melbourne (TM) [10] and the Urbana IX 3NF [11]. The TM 3NF was recently updated and now respects chiral symmetry, as noted in Refs. [12,13]. Therefore we will also use the newest version from [14], called TM′(99). One can simultaneously achieve the correct binding energies for the three-nucleon and four-nucleon systems by including the TM and Urbana IX 3NFs into the nuclear Hamiltonian. In addition, adding the Urbana IX 3NF, provides a fair description of the low energy bound-state energies up to $A=10$ nuclei. Recently, this description has been significantly improved by augmenting the Hamiltonian by the Illinois 3NFs, which are based on three-pion exchanges with intermediate Δ's [15].

The binding energies of *s*-shell nuclei show the significance of 3NFs, but they only constrain their overall strength.

*Electronic address: kimiko@rarfaxp.riken.go.jp

The binding energies of p-shell nuclei provide additional features. In order to unambiguously clarify the detailed properties of 3NFs at least for a total isospin of $T=1/2$, the investigation of three-nucleon scattering processes is required. A rich set of energy dependent spin observables and differential cross sections are available for those reactions. Theoretical calculations based on several NN and $3N$ interaction models provide the theoretical guidance for selecting specific observables and energies, which will appropriately determine the 3NF properties. The rapid progress in supercomputer technology has made it possible to achieve numerically exact solutions for the Faddeev equations up to an incident nucleon laboratory energy of 200 MeV using present day two-nucleon ($2N$) and three-nucleon ($3N$) potentials. The first clear signatures of 3NF effects in the $3N$ continuum came from a study of minima in the differential cross section for nucleon-deuteron (Nd) elastic scattering at incoming nucleon energies above ≈ 60 MeV [16]. Including the 2π-exchange TM 3NF in the nuclear Hamiltonian removed a large part of the discrepancy between data and theoretical predictions. Calculations of Nd scattering in a coupled-channel approach, where Δ-isobar degrees of freedom were explicitly included, supported this conclusion [17]. All these results confirm that Nd elastic scattering is a good tool for exploring the 3NF properties in this energy region.

The developments and progress in technology of highly polarized proton and deuteron ion sources and their application in recently constructed accelerators as well as new sophisticated techniques for target polarization, make it possible to obtain very precise data for the spin observables at high energies ($E/A \gtrsim 60$ MeV). Constructing highly efficient polarimeters has also allowed accurate measurements of spin polarization-transfer observables [18,19]. In Refs. [18,20,21] we have reported precise data for the cross section and all deuteron analyzing powers for d-p elastic scattering at incoming deuteron energies of 70, 100, and 135 MeV/nucleon. The data are compared with theoretical predictions based on various realistic NN potentials combined with different 3NFs, namely with the 2π-exchange TM 3NF model, with a modification thereof, (TM$'$) [12,13,22], with the Urbana IX 3NF, and with the phenomenological spin-orbit 3NF [23]. For almost all observables, clear discrepancies between the data and $2N$ force only predictions are found, especially in the cross section minima, which increase with incident deuteron energy. For the cross section, accounting for the 3NFs, essentially removes these discrepancies. For the deuteron vector analyzing power A_y^d, the 3NFs successfully explain the difference between the data and the $2N$ force only theoretical predictions. Note that adding TM 3NF reproduces the recent data for A_y^d and the spin-correlation coefficient $C_{y,y}$ at 197 MeV by Cadman *et al.* [24]. However, theoretical predictions that incorporate 3NFs (TM, TM$'$ and Urbana IX 3NFs) do not reproduce the deuteron tensor analyzing power data. Recent proton vector analyzing power data have also revealed the deficiency of the 2π-exchange TM 3NF model [24–27] that yields large, incorrect effects. The Urbana IX and TM$'$ 3NFs are much more successful and provide a better description [27,28].

In the present study, we extend our measurement to new observables, deuteron-to-proton $(\vec{d}+p \rightarrow \vec{p}+d)$ polarization-transfer coefficients $K_y^{y'}$, $K_{xx}^{y'}-K_{yy}^{y'}$ ($K_{xx}^{y'}$, $K_{yy}^{y'}$), and $K_{xz}^{y'}$ at 135 MeV/nucleon in the region of c.m. angles $\theta_{c.m.}=90°-180°$. These spin-transfer coefficients are predicted to have strong sensitivities to the current 3NF models [28]. This is the first measurement of such polarization-transfer coefficients in this energy range ($E/A \gtrsim 60$ MeV). To the best of our knowledge, only proton-to-proton polarization-transfer coefficients have been measured, but at a much higher energy [19]. The present data will provide a sensitive test for the 3NF models in elastic d-p scattering below the pion production threshold energy.

In Sec. II the details of our experimental arrangement are presented. In Sec. III we provide a description of the data analysis and experimental results. In Sec. IV we briefly review the basics of the $3N$ scattering formalism and gives a short description of the 3NFs used in this study. Our experimental results are compared with the theoretical predictions in Sec. V, while Sec. VI contains the summary and conclusion.

II. EXPERIMENTAL PROCEDURE

A. Polarized deuteron beams and target

The experiments were performed at the RIKEN Accelerator Research Facility (RARF) using the SMART system [29] including the focal plane polarimeter DPOL [30]. The atomic beam type RIKEN polarized ion source [31] provided the vector and tensor polarized deuteron beams. In the present measurements the data were taken with the vector and tensor polarization modes of the polarized and unpolarized deuteron beams given in terms of the theoretical maximum polarization values as $(\mathcal{P}_Z,\mathcal{P}_{ZZ})=(0,0)$, $(0,-2)$, $(-2/3,0)$ and $(1/3,1)$. These polarization modes were cycled in 5-second intervals by switching the rf transition units of the ion source. The deuteron polarization axis was rotated by a spin rotation system Wien Filter [32] prior to acceleration. It was perpendicular to the scattering plane when measuring $K_y^{y'}$ and $K_{yy}^{y'}$. For $K_{xx}^{y'}$, the rotation was performed into the scattering plane so that the polarization axis pointed sideways, perpendicular to the beam. For the $K_{xz}^{y'}$ measurement, the spin symmetry axis was additionally rotated in the reaction plane and aligned at an angle β to the beam direction. A typical value of β was $131.6°\pm0.2°$. The beam polarization was monitored by d-p elastic scattering at 135 MeV/nucleon and it was 60–80% of the theoretical maximum values throughout the measurement. Polyethylene (CH$_2$) with a thickness of 90-mg/cm^2 or liquid hydrogen with a thickness of 20-mg/cm^2, employed as a hydrogen target (^{1}H) [33], was bombarded with a beam intensity of 10–60 nA.

B. Beam-line polarimeter

Two sets of beam-line polarimeters monitored the beam polarization. The first, the D-room polarimeter, was installed downstream of the Ring cyclotron, which was used to determine the beam polarization after the deuterons were accelerated by the Ring cyclotron. The second, the Swinger polarimeter (see Fig. 1), was placed in front of the scattering
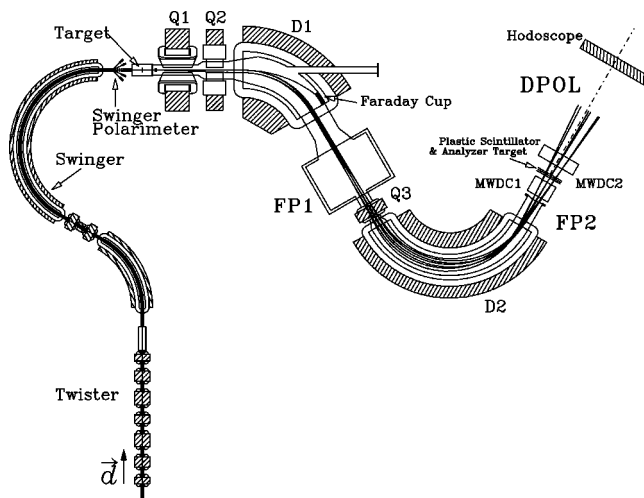
FIG. 1. Arrangement of the RIKEN Spectrograph SMART. The FP1 and FP2 denote the first and second focal planes, respectively. Scattered protons were momentum analyzed by the magnetic spectrograph and detected at the FP2. The polarization of the scattered protons was measured with the focal-plane polarimeter DPOL.

chamber in the experimental room. Since the incident beam direction was rotated using the beam-swinger system of SMART, the polarization axis of the beam was precessed during the beam transportation from the D-room polarimeter to the target position. The Swinger polarimeter moved with the beam swinger so that this polarimeter could directly measure the beam polarization at the target. The beam polarization before and after each run was measured using the Swinger polarimeter.

The polarimetry was made by using the analyzing powers for d-p elastic scattering. To obtain the absolute values of the deuteron beam polarizations, the analyzing powers for d-p elastic scattering were calibrated by using the ^{12}C(d,α)^{10}B*[2$^+$] reaction, the $A_{yy}(0°)$ of which is exactly $-1/2$ because of parity conservation [34]. A CH$_2$ sheet was the target for each polarimeter. The target thickness was 270-mg/cm^2 for the D-room polarimeter and 90-mg/cm^2 for the Swinger polarimeter. Each polarimeter consisted of four pairs of 1-cm thick plastic scintillators placed symmetrically in left, right, up and down directions. The scattered deuterons and recoil protons were detected in a kinematical coincidence. This setup reduced background events due to the deuteron breakup process or the inelastic scattering from carbon nuclei.

C. SMART system and focal plane polarimeter DPOL

The polarization-transfer measurement was performed using the SMART system [29] with the focal-plane polarimeter DPOL [30] (see Fig. 1). The polarized deuteron beam bombarded the hydrogen target placed in the scattering chamber. Recoil protons were momentum analyzed by the magnetic spectrograph and detected at its second focal plane (FP2 in Fig. 1). In the SMART system, the magnetic spectrograph was fixed to the ground and the incident beam direction was rotated by the Swinger magnet, leading to a vertical reaction plane.

The FP2 detector system consisted of a multi-wire drift chamber (MWDC1 in Fig. 2) and three plastic scintillation counters (SC1-3 in Fig. 2). The MWDC1 was used to reconstruct the trajectories of the particles at the FP2. The configuration of the wire planes was X-Y-X'-Y'-X'-Y'-X-Y and the coordinate frames were defined as follows. The z-axis referred to the central ray. The x-axis was perpendicular to the
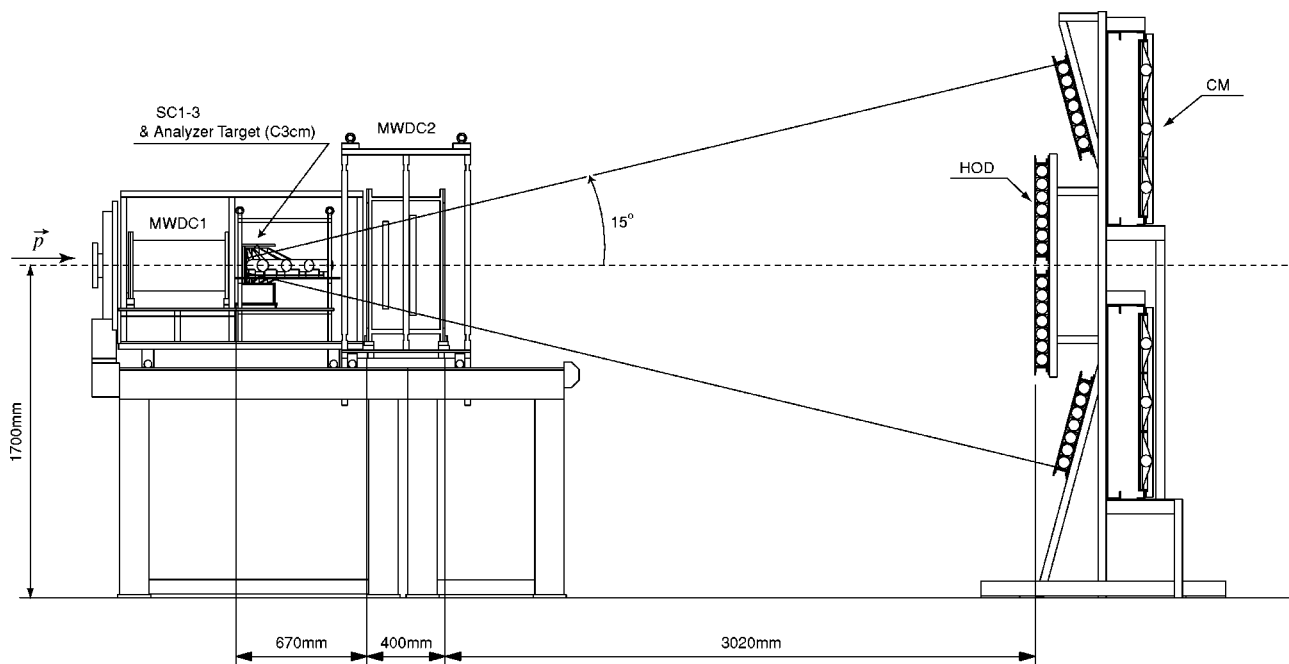

FIG. 2. Second-focal-plane detector system including the focal-plane polarimeter DPOL. It consists of two multiwire drift chambers (MWDC1 and MWDC2), plastic scintillation trigger counters (SC1, SC2, SC3), a polarization analyzer target, and a counter hodoscope system (HOD and c.m.).

z-axis in the horizontal plane and the y-axis was taken as $\hat{x} \times \hat{z}$. All position sensitive planes were normal to the z-axis and separated by a distance of 50 mm from adjacent planes. The planes with primes were displaced half a cell relative to the unprimed ones which helped solve the so-called left-right ambiguity. The cell size was 20 mm × 20 mm for the X-planes and 10 mm × 10 mm for the Y-planes. The plastic scintillation counters BICRON BC-408 of the size 108 mm^H × 800 mm^W × 5 mm^T (SC1-3 in Fig. 2) were used to identify proton events scattered from the hydrogen target and to generate event triggers. The photo-multiplier tubes Hamamatsu H1161 were placed at both ends of the scintillators via light guides.

The proton polarization was measured by DPOL after momentum analysis in the magnetic spectrograph. The DPOL consisted of an analyzer target, a multi-wire drift chamber (MWDC2 in Fig. 2), and a counter hodoscope system (HOD and c.m. in Fig. 2). The DPOL was primarily designed and optimized for the deuteron polarization measurements and then was modified to measure the proton polarization.

The polarimetry was made using $p+C$ scattering. As an analyzer target, a 3-cm thick carbon plate was sandwiched between two plastic scintillation trigger counters (SC1 and SC2 in Fig. 2). The trajectories of the scattered protons from the $p+C$ reaction were reconstructed by the MWDC2. The MWDC2 was 670 mm downstream from the exit window of the MWDC1 and had eight layers of sense-wire planes with the Y_f-Y_f'-X_f-X_f'-Y_r-Y_r'-X_r-X_r' configuration. Here "f" and "r" denote the front and rear planes, respectively. The planes with primes were, again, displaced half a cell relative to the unprimed ones. The coordinate frame was defined as in the case of the MWDC1. The cell size was 14 mm × 14 mm (15 mm × 15 mm) for the $X_f(X_r)$ planes and 14 mm × 14 mm(16 mm × 16 mm) for the $Y_f(Y_r)$ planes. The number of cells was 64 for the X-planes and 32 for the Y-planes.

Event triggers for proton events from the $p+C$ reaction were generated by making a coincidence of the signals of the SC1–3 counters and those of the counter hodoscope system which was located 4 m downstream from the analyzer target. The angular range covered by the hodoscope system was ±15° both vertically and horizontally. The unscattered protons passed through the insensitive region between the upper and lower parts of the hodoscope. The front wall of the hodoscope (HOD in Fig. 2) was comprised of a layer of 28 segmented plastic scintillators, which were 2200-mm wide, 65-mm high and 65-mm thick. The light output signals from each HOD were read out by two photo-multiplier tubes Hamamatsu H1161 that were directly coupled to each scintillator at both ends. The rear wall consisted of six plastic scintillators (c.m. in Fig. 2). Each c.m. counter was 2200-mm wide, 190-mm high and 10-mm thick. Two photo-multiplier tubes Hamamatsu H1161 were attached to both ends of each scintillation counter via light guides. In the angular range $\theta_{c.m.} = 120° - 180°$ for d-p elastic scattering, the c.m. counters were used to generate the $p+C$ event triggers by taking the coincidence with the HOD and SC1-3 signals. However, for angles $\theta_{c.m.} = 90° - 110°$ the kinetic energies of the scattered protons were too low to allow them to reach the c.m. counters. Under these circum-
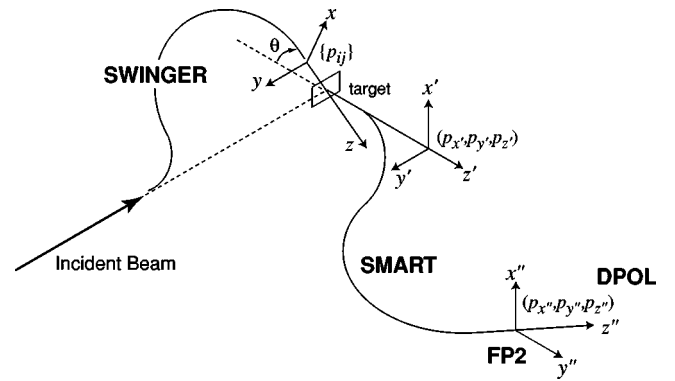

FIG. 3. Definition of the Coordinate Frame for the SMART system. The $\{p_{ij}\}$ denotes the vector or tensor deuteron beam polarizations. The $p_{i'}$ is the polarization of the scattered protons and the $p_{i''}$ is the polarization of the scattered protons at the second focal plane FP2.

stances, the c.m. signals were not used as the event trigger.

Data acquisition was carried out with a fast data-acquisition system for the SMART spectrograph [35]. The data were accumulated in a VME memory module through the FERA bus and then DMA-transferred to a personal computer.

III. DATA ANALYSIS AND EXPERIMENTAL RESULTS

A. Polarization-transfer coefficients

1. Coordinate frame for the polarization observables at the SMART system

The coordinate frame for the polarization observables in the SMART system is defined according to the Madison convention [36], shown in Fig. 3. The z-axis is given by the beam direction. The y-axis is perpendicular to the reaction plane and the x-axis is defined by $\hat{y} \times \hat{z}$. The coordinate system (x', y', z') for the polarization of the scattered protons is rotated through the dipole magnet of the SMART spectrograph into the coordinate system at FP2 (x'', y'', z'').

In Fig. 3, $\{p_{ij}\}$ is the vector or tensor deuteron beam polarization, $p_{i'}$ is the polarization of the scattered protons and $p_{i''}$ is the polarization of the scattered protons at FP2. In the present measurement, $p_{y''}$ was measured with the focal-plane polarimeter DPOL and $p_{y'}$ was extracted using $p_{y''}$ and the spin precession angle χ in the dipole magnets of the spectrometer (see Sec. III A 2).

2. Effective analyzing power measurement

The effective analyzing powers A_y^C of DPOL were calibrated at three proton energies 120, 144, and 200 MeV which almost covered the kinetic energy region of scattered protons for d-p elastic scattering ($E_p^{scatt.} = 120 - 240$ MeV). Since polarized proton beams were unavailable at RARF, the induced polarization $P^{y'}$ in the $^{12}C(p, \vec{p})^{12}C$ elastic scattering was used to determine A_y^C. The analyzing powers A_y for the time-reversed reaction $^{12}C(\vec{p}, p)^{12}C$ are equal to the induced polarizations $P^{y'}$ and were precisely measured at $E_p = 122$

and 200 MeV by Meyer *et al.* at IUCF [37,38]. For 200 MeV, the calibrations were performed by using the two spin modes of the polarized proton beams obtained by the ^{12}C($p,\vec{p}$)^{12}C elastic scattering at $\theta_{\text{lab.}}=16.1°$ and 28.1°. The expected values of the polarizations $P^{y'}$ were 0.993 and -0.425 for the $\theta_{\text{lab.}}=16.1°$ and 28.1°, respectively. For 120 MeV, the calibration was performed at the angle $\theta_{\text{lab.}}=24.2°$ where the polarization of the proton beams was expected to be 0.715. Passing 200 MeV proton beams through a brass plate, which was in front of the MWDC1 just downstream of the exit window of the D2 magnet, reduced the energy to create 144 MeV polarized proton beams. A 284 -mg/cm^2 thick graphite target in the SMART scattering chamber was bombarded by unpolarized proton beams and the scattered protons bombarded the polarization analyzer target. Since the y''-axis is in the horizontal plane in the SMART system (see Fig. 3), the up-down asymmetry was used to extract the effective analyzing power A_y^C. The A_y^C is given by

$$A_y^C = \frac{\int_{-\Delta\phi}^{\Delta\phi}\int_{\theta_{\min}}^{\theta_{\max}} I_0(\theta)A_y(\theta)\sin\theta\cos\phi\,d\theta d\phi}{\int_{-\Delta\phi}^{\Delta\phi}\int_{\theta_{\min}}^{\theta_{\max}} I_0(\theta)\sin\theta\,d\theta d\phi}. \quad (1)$$

The numbers of events in the upper, N_U, and lower, N_D, side region are obtained as

$$N_U = \int_{-\Delta\phi}^{\Delta\phi}\int_{\theta_{\min}}^{\theta_{\max}} I_0(\theta)[1+A_y(\theta)p_{y''}\cos\phi]\sin\theta\,d\theta d\phi, \quad (2)$$

$$N_D = \int_{-\Delta\phi+\pi}^{\Delta\phi+\pi}\int_{\theta_{\min}}^{\theta_{\max}} I_0(\theta)[1+A_y(\theta)p_{y''}\cos\phi]\sin\theta\,d\theta\,d\phi. \quad (3)$$

Here, $I_0(\theta)$ and $A_y(\theta)$ are the cross section and the analyzing power for inclusive proton scattering in the carbon analyzer of DPOL. The $p_{y''}$ is the proton beam polarizations at the FP2 shown in Fig. 3. To reduce instrumental asymmetries, A_y^C was extracted in the following way. From Eqs. (1)–(3) N_U and N_D were normalized as

$$n_U \equiv \frac{N_U}{N_U+N_D} = \frac{1}{2}(1+A_y^C p_{y''}), \quad (4)$$

$$n_D \equiv \frac{N_D}{N_U+N_D} = \frac{1}{2}(1-A_y^C p_{y''}). \quad (5)$$

The spin-up ($p_{y''}^+;p_{y''}>0$) and spin-down ($p_{y''}^-;p_{y''}<0$) polarized proton beams used in the measurement together with the corresponding $n_U^\pm$ and $n_D^\pm$ provide the effective analyzing power A_y^C as
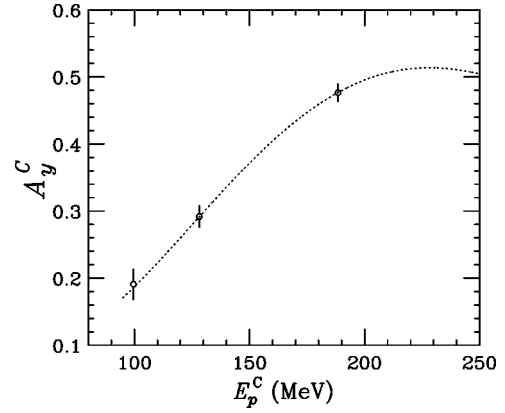

FIG. 4. Energy dependence of the effective analyzing power A_y^C of DPOL and the measured data.

$$A_y^C = \frac{(n_U^+ - n_D^+)-(n_U^- - n_D^-)}{p_{y''}^+ - p_{y''}^-}. \quad (6)$$

In the 120 MeV measurements, the data were collected with the one-mode polarized proton beams. Therefore, in the analysis we also used the data with unpolarized beams, which were obtained by directly tuning the incident proton beams onto the polarization analyzer target at the focal plane. Angular integrations in Eqs. (2) and (3) were performed over regions of polar and azimuthal angles of $5°\leqslant\theta\leqslant15°$ and $\Delta\phi=60°$, respectively. The proton spin precessed around the vertical axis of the spectrometer and the spin precession angle χ with respect to the direction of the proton momentum is given in the moving frame by $\chi=\gamma(g/2-1)\Theta_D$, where γ is the Lorentz factor $\gamma=(m_pc^2+E_p)/m_pc^2$, g is the spin g factor of the proton, and Θ_D is the bending angle of the spectrometer. The total bending angle of the magnetic spectrograph is $\Theta_D=60°$. Thus $p_{y''}$ is given as

$$p_{y''} = P^{y'}\cos\chi. \quad (7)$$

Figure 4 shows the measured effective analyzing power A_y^C with open circles as a function of the proton energy at the center of the carbon plate E_p^C. Only the statistical errors are shown. The E_p^C was calculated by numerically integrating the energy loss per unit thickness described by the Bethe-Bloch equations. The energy dependent curve of A_y^C was obtained by fitting the effective analyzing powers calculated from the empirical-energy-dependent fit of the inclusive analyzing powers for $p+$C by McNaughton *et al.* [39] and the angular distributions of the differential cross section of Aprile-Giboni *et al.* [40]. The obtained curve was scaled to adjust the experimentally obtained A_y^C (the dotted curve in Fig. 4). The uncertainty of the input parameters for the $p+$C inclusive analyzing power [39] is 2%. The uncertainty of the fit for the energy dependent curve is 6%, in which the scaling factor has an uncertainty of 2%. Thus, the estimated overall systematic uncertainty of the effective analyzing power, A_y^C, of DPOL is 7%.

3. Extraction of the polarization observables

The polarization-transfer coefficients for the reaction $\vec{d} + p \rightarrow \vec{p} + d$ are expressed through the unpolarized (σ_0) and polarized (σ) cross sections together with the polarizations of incoming deuterons (p_{ij}) and outgoing protons ($p_{k'}$) as

$$p_{x'}\sigma/\sigma_0 = \frac{3}{2}p_x K_x^{x'} + \frac{3}{2}p_z K_z^{x'} + \frac{2}{3}p_{xy}K_{xy}^{x'} + \frac{2}{3}p_{yz}K_{yz}^{x'}, \quad (8)$$

$$p_{y'}\sigma/\sigma_0 = P^{y'} + \frac{3}{2}p_y K_y^{y'} + \frac{2}{3}p_{xz}K_{xz}^{y'}$$
$$+ \frac{1}{3}\left(p_{xx}K_{xx}^{y'} + p_{yy}K_{yy}^{y'} + p_{zz}K_{zz}^{y'}\right), \quad (9)$$

$$p_{z'}\sigma/\sigma_0 = \frac{3}{2}p_x K_x^{z'} + \frac{3}{2}p_z K_z^{z'} + \frac{2}{3}p_{xy}K_{xy}^{z'} + \frac{2}{3}p_{yz}K_{yz}^{z'}, \quad (10)$$

where x, y, and z (x', y', and z') are the coordinate systems used to describe the polarization of the incident deuterons (outgoing protons) [36].

To extract the polarization-transfer coefficients $K_y^{y'}$, $K_{xx}^{y'}$, $K_{yy}^{y'}$, and $K_{xz}^{y'}$, we used the polarized deuteron beams with the spin symmetry axis directed in the optimum orientation for each observable. We rotated it to the y-axis for $K_y^{y'}$ and $K_{yy}^{y'}$, and to the x-axis for the $K_{xx}^{y'}$ measurement. For the $K_{xz}^{y'}$ measurement we rotated the spin symmetry axis into the reaction plane and additionally aligned it at an angle β to the beam direction ($\beta = 131.6° \pm 0.2°$). To obtain $K_{xx}^{y'} - K_{yy}^{y'}$, $K_{xx}^{y'}$ and $K_{yy}^{y'}$ were independently measured. Accordingly the polarized cross section can be written for each observable as

$$p_{y'}\sigma/\sigma_0 = P^{y'} + \frac{3}{2}p_y K_y^{y'} + \frac{1}{2}p_{yy}K_{yy}^{y'}, \quad \text{for } K_y^{y'} \text{ and } K_{yy}^{y'}, \quad (11)$$

$$p_{y'}\sigma/\sigma_0 = P^{y'} + \frac{1}{2}p_{xx}K_{xx}^{y'}, \quad \text{for } K_{xx}^{y'}, \quad (12)$$

$$p_{y'}\sigma/\sigma_0 = P^{y'} + \frac{2}{3}p_{xz}K_{xz}^{y'} + \frac{1}{3}(p_{xx} - p_{zz})K_{xx}^{y'}$$
$$+ \frac{1}{3}(p_{yy} - p_{zz})K_{yy}^{y'}, \quad \text{for } K_{xz}^{y'}, \quad$$

$$\text{with} \quad K_{xx}^{y'} + K_{yy}^{y'} + K_{zz}^{y'} = 0. \quad (13)$$

By using the relation between the deuteron beam polarizations ($\mathcal{P}_Z, \mathcal{P}_{ZZ}$) (see Sec. II A) and ($p_i, p_{lk}$) given by the angles ($\beta, \phi$) [36] and the relation $p_{y''} = p_{y'}\cos\chi$ (see Sec. III A 2), the polarized cross section for each polarization-transfer coefficient given in Eqs. (11)–(13) is expressed as

$$p_{y''}\sigma/\sigma_0 = p_{y'}\sigma/\sigma_0 \cos\chi$$
$$= (P^{y'} + v_e\mathcal{P}_Z + t_e\mathcal{P}_{ZZ})\cos\chi$$
$$= \mathcal{P}^{y'} + \mathcal{V}_e\mathcal{P}_Z + \mathcal{T}_e\mathcal{P}_{ZZ}, \quad (14)$$

where

$$\mathcal{P}^{y'} = P^{y'}\cos\chi. \quad (15)$$

For $K_y^{y'}$ and $K_{yy}^{y'}$, the $\mathcal{V}_e$ and $\mathcal{T}_e$ are given as

$$\mathcal{V}_e = \frac{3}{2}K_y^{y'}\cos\phi\sin\beta\cos\chi, \quad (16)$$

$$\mathcal{T}_e = \frac{1}{2}K_{yy}^{y'}(\sin^2\beta\cos^2\phi - \cos^2\beta)\cos\chi = \frac{1}{2}K_{yy}^{y'}\cos\chi, \quad (17)$$

where $(\beta, \phi) = (90°, 0°)$.
For $K_{xx}^{y'}$,

$$\mathcal{T}_e = \frac{1}{2}K_{xx}^{y'}(\sin^2\beta\sin^2\phi - \cos^2\beta)\cos\chi = \frac{1}{2}K_{xx}^{y'}\cos\chi, \quad (18)$$

where $(\beta, \phi) = (90°, -90°)$.
For $K_{xz}^{y'}$,

$$\mathcal{T}_e = \left\{ -K_{xz}^{y'}\sin\beta\cos\beta\sin\phi + \frac{1}{2}K_{xx}^{y'}(\sin^2\beta\sin^2\phi - \cos^2\beta) \right.$$
$$\left. + \frac{1}{2}K_{yy}^{y'}(\sin^2\beta\cos^2\phi - \cos^2\beta) \right\}\cos\chi. \quad (19)$$

It should be noted that the $K_{xz}^{y'}$ value was extracted using the measured $K_{xx}^{y'}$ and $K_{yy}^{y'}$ values.

The $p_{y''}$ is obtained from Eqs. (2) and (3) as

$$p_{y''} = \frac{A_{\text{sym.}}}{A_y^C}, \quad$$

$$A_{\text{sym.}} \equiv \frac{N_U - N_D}{N_U + N_D}. \quad (20)$$

From the resulting values of $p_{y''}^{(i)}$ for each spin-mode ♯i (see Sec. II A), the $\mathcal{P}^{y'}$, $\mathcal{V}_e$, and $\mathcal{T}_e$ values were calculated as

$$\mathcal{P}_{[1]}^{y'} = p_{y''}^{(0)}, \quad (21)$$

$$\mathcal{P}_{[2]}^{y'} = \{p_{y''}^{(1)}R^{(1)}(\mathcal{P}_Z^{(2)}\mathcal{P}_{ZZ}^{(3)} - \mathcal{P}_Z^{(3)}\mathcal{P}_{ZZ}^{(2)}) + p_{y''}^{(2)}R^{(2)}(\mathcal{P}_Z^{(3)}\mathcal{P}_{ZZ}^{(1)}$$
$$- \mathcal{P}_Z^{(1)}\mathcal{P}_{ZZ}^{(3)}) + p_{y''}^{(3)}R^{(3)}(\mathcal{P}_Z^{(1)}\mathcal{P}_{ZZ}^{(2)} - \mathcal{P}_Z^{(1)}\mathcal{P}_{ZZ}^{(2)})\}/\{(\mathcal{P}_Z^{(2)}\mathcal{P}_{ZZ}^{(3)}$$
$$- \mathcal{P}_Z^{(3)}\mathcal{P}_{ZZ}^{(2)}) + (\mathcal{P}_Z^{(3)}\mathcal{P}_{ZZ}^{(1)} - \mathcal{P}_Z^{(1)}\mathcal{P}_{ZZ}^{(3)}) + (\mathcal{P}_Z^{(1)}\mathcal{P}_{ZZ}^{(2)}$$
$$- \mathcal{P}_Z^{(1)}\mathcal{P}_{ZZ}^{(2)})\}, \quad (22)$$

$$\mathcal{V}_e = \left[p_{y''}^{(2)} - p_{y''}^{(3)} - \mathcal{A}_T p_{y''}^{(1)} - \left\{ \frac{1}{R^{(2)}} - \frac{1}{R^{(3)}} \right. \right.$$
$$\left. \left. - \mathcal{A}_T \frac{1}{R^{(1)}} \right\} p_{y''}^{(0)} \right] \bigg/ \left\{ \frac{\mathcal{P}_Z^{(2)}}{R^{(2)}} - \frac{\mathcal{P}_Z^{(3)}}{R^{(3)}} - \mathcal{A}_T \frac{\mathcal{P}_Z^{(1)}}{R^{(1)}} \right\}, \quad (23)$$

$$\mathcal{T}_e = \left[p_{y''}^{(1)} - p_{y''}^{(3)} - \mathcal{A}_V p_{y''}^{(2)} - \left\{ \frac{1}{R^{(1)}} - \frac{1}{R^{(3)}} \right. \right.$$
$$\left. \left. - \mathcal{A}_V \frac{1}{R^{(2)}} \right\} p_{y''}^{(0)} \right] \bigg/ \left\{ \frac{\mathcal{P}_{ZZ}^{(1)}}{R^{(1)}} - \frac{\mathcal{P}_{ZZ}^{(3)}}{R^{(3)}} - \mathcal{A}_V \frac{\mathcal{P}_{ZZ}^{(2)}}{R^{(2)}} \right\},$$
$$(24)$$

where

$$\mathcal{A}_V = \frac{R^{(2)}}{\mathcal{P}_Z^{(2)}} \left\{ \frac{\mathcal{P}_Z^{(1)}}{R^{(1)}} - \frac{\mathcal{P}_Z^{(3)}}{R^{(3)}} \right\}, \quad (25)$$

$$\mathcal{A}_T = \frac{R^{(1)}}{\mathcal{P}_{ZZ}^{(1)}} \left\{ \frac{\mathcal{P}_{ZZ}^{(2)}}{R^{(2)}} - \frac{\mathcal{P}_{ZZ}^{(3)}}{R^{(3)}} \right\}, \quad (26)$$

with $R^{(i)} = \sigma^{(i)}/\sigma_0$.

The induced polarization was obtained using $\mathcal{P}_{[1]}^{y'}$, $\mathcal{P}_{[2]}^{y'}$ in Eqs. (21) and (22), respectively, and the resulting values were consistent with each other within statistical accuracy. Finally, $P_{[1]}^{y'}$ and $P_{[2]}^{y'}$ averaged with the statistical weights were used to minimize the errors when determining the $P^{y'}$ value.

Figure 5 shows the excitation energy spectra at the angles $\theta_{c.m.} = 176.8°$, $120.0°$, and $90.0°$ obtained with the liquid hydrogen target. At $\theta_{c.m.} = 176.8°$, the portion of the spectrum due to the final-state interaction (FSI) of the d-p breakup reaction is clearly seen at energies $E_x \gtrsim 2$ MeV and it is well separated from d-p elastic scattering events. The kinetic energy of the outgoing proton for d-p elastic scattering changes rapidly with scattering angle and the energy resolution deteriorates at forward angles in the c.m. system. Therefore, spectra due to elastic scattering and breakup reactions are not clearly separated at angles $\theta_{c.m.} \leqslant 140°$ (see the spectra for $\theta_{c.m.} = 120°$ and $90°$ in Fig. 5). To reduce the background, only events in the hatched region were selected to obtain the polarization observables for d-p elastic scattering. The position of the hatched energy region did not include the energy region $E_x \gtrsim 2$ MeV, that is clearly dominated by the breakup reaction. To see the background contributions for energies $E_x \leqslant 2$ MeV, the polarization was obtained by changing the maximum energy value in the hatched energy region. The magnitude of the polarization values changed by 0.02 or less. Typically, an integration range $E_x \leqslant 0.5$ MeV was adopted to extract the final polarization observables.

The experimental results for the polarization-transfer coefficients ($K_y^{y'}$, $K_{yy}^{y'}$, $K_{xx}^{y'}$, and $K_{xz}^{y'}$) and the induced proton polarization $P^{y'}$ are shown with open circles in Fig. 6 and are tabulated in Table I. Only the statistical uncertainties are
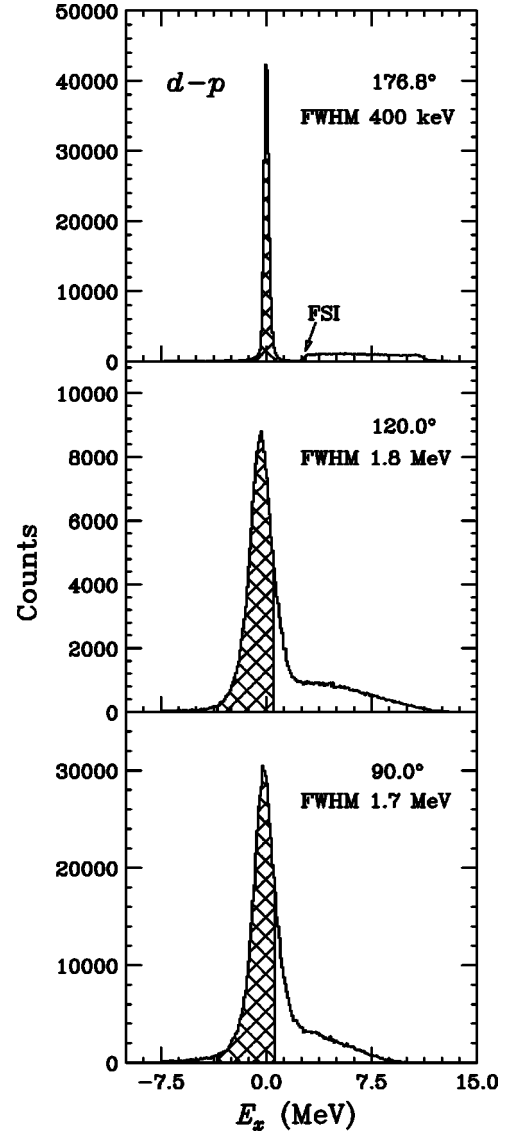

FIG. 5. Excitation energy spectra for d-p elastic scattering at c.m. angles $\theta_{c.m.} = 176.8°$, $120°$, and $90°$ taken with the liquid hydrogen target.

shown and their magnitudes are less than 0.02 for $P^{y'}$ and less than 0.03 for all polarization-transfer coefficients ($K_y^{y'}$, $K_{yy}^{y'}$, $K_{xx}^{y'}$, $K_{xz}^{y'}$).

The chance of the polarization-transfer coefficients due to the uncertainty of the bending angle of the spectrometer is less than 1%. The uncertainty of the effective analyzing power for DPOL is 7%. The deuteron beam polarizations have an uncertainty of less than 3%. The effect of the breakup reaction at angles $\theta_{c.m.} \leqslant 140$ MeV, where the events were inseparable from the elastic ones, was 0.02. Therefore the systematic uncertainties associated with the breakup reaction did not override the statistical ones. The overall systematic uncertainties are estimated to be about 8% for the polarization-transfer coefficients and the induced polarization $P^{y'}$. For the induced polarization $P^{y'}$, our data were compared with the proton analyzing power A_y^p for p-d elastic scattering measured at KVI [27] (solid squares in Fig. 6).
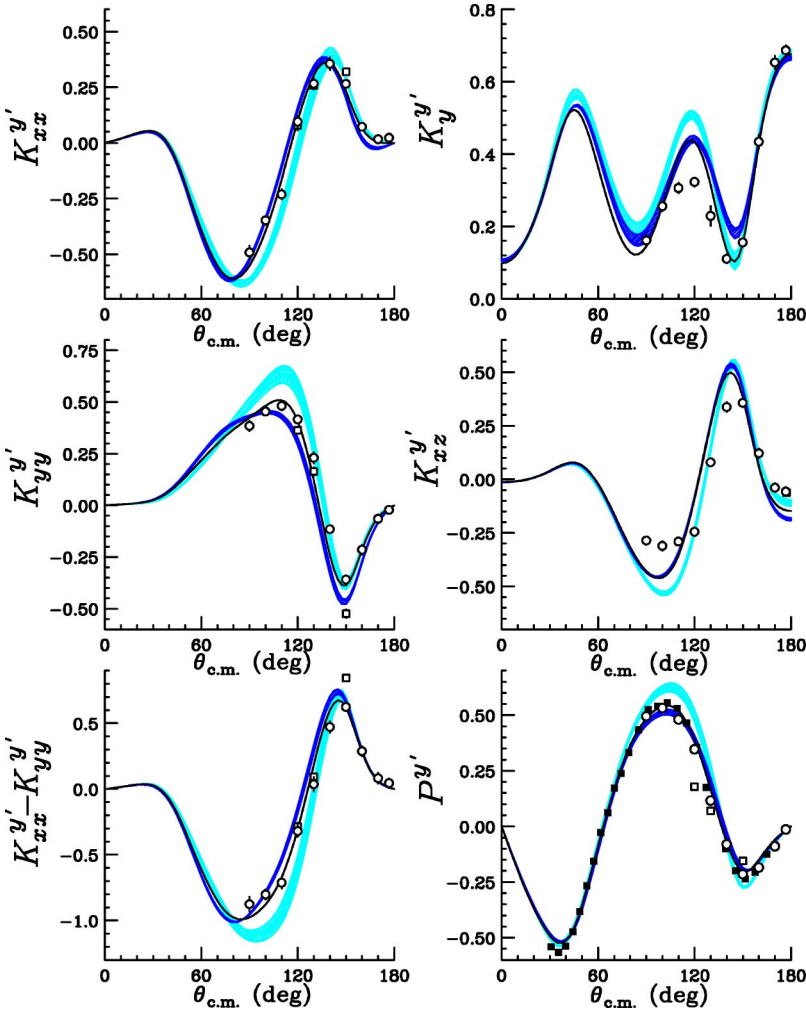
FIG. 6. (Color online) polarization-transfer coefficients $K_{xx}^{y'}$, $K_{yy}^{y'}$, $K_{xx}^{y'}-K_{yy}^{y'}$, $K_{y}^{y'}$, $K_{xz}^{y'}$, and the induced polarization $P^{y'}$ in elastic d-p scattering at the incident deuteron energy of 135 MeV/nucleon. Open circles are the data in the present measurement and open squares are the data in the test measurement (Ref. [18]). Solid squares on the $P^{y'}$ figure are the proton analyzing power data for the time-reversed reaction ^{2}H($\vec{p},p$)^{2}H (Ref. [27]). The light shaded bands contain the *NN* force predictions (AV18, CD-Bonn, Nijmegen I, II and 93), and the dark shaded bands contain the combinations of the *NN*+TM′(99) 3NF predictions as described in the text. The solid curve is the AV18+Urbana IX 3NF prediction.

Assuming time-reversal invariance $P^{y'} = -A_y^p$, and these two independent measurements agree with each other within the statistical uncertainties in the measured angular range $\theta_{c.m.} = 90° - 180°$. Figure 6 shows the data obtained in the test measurement [18] (open circles) together with the present data. These two measurements are consistent, except for $K_{yy}^{y'}$ at $\theta_{c.m.} = 150°$.

B. Analyzing powers

As described in Sec. II B, the analyzing powers for d-p elastic scattering were used to obtain the deuteron beam polarizations. Recently, to determine the absolute values of the beam polarizations, the analyzing powers for d-p elastic scattering were calibrated at six angles for deuteron energies of 70 and 135 MeV/nucleon, by using the reaction

TABLE I. Data table for d-p elastic scattering deuteron-to-proton polarization-transfer coefficients and induced proton polarizations at 135 MeV/nucleon.

$\theta_{c.m.}$ (deg)	$P^{y'}$	$\delta P^{y'}$	$K_y^{y'}$	$\delta K_y^{y'}$	$K_{yy}^{y'}$	$\delta K_{yy}^{y'}$	$K_{xx}^{y'}$	$\delta K_{xx}^{y'}$	$K_{xz}^{y'}$	$\delta K_{xz}^{y'}$
90.0	0.495	0.010	0.162	0.017	0.385	0.026	−0.492	0.031	−0.286	0.018
100.0	0.532	0.013	0.256	0.014	0.454	0.020	−0.348	0.020	−0.310	0.023
110.0	0.481	0.015	0.306	0.015	0.482	0.022	−0.231	0.023	−0.290	0.019
120.0	0.347	0.008	0.323	0.013	0.416	0.016	0.096	0.027	−0.245	0.021
130.0	0.116	0.008	0.229	0.027	0.230	0.028	0.267	0.027	0.080	0.020
140.0	−0.080	0.009	0.111	0.013	−0.115	0.015	0.356	0.029	0.338	0.022
150.0	−0.214	0.010	0.156	0.012	−0.359	0.015	0.266	0.015	0.358	0.021
160.0	−0.185	0.006	0.434	0.019	−0.215	0.024	0.073	0.015	0.122	0.023
170.0	−0.089	0.006	0.654	0.019	−0.065	0.021	0.017	0.020	−0.039	0.022
176.8	−0.014	0.005	0.687	0.014	−0.022	0.015	0.023	0.021	−0.057	0.021

TABLE II. Calibrated analyzing power data for d-p elastic scattering at 70 MeV/nucleon reported in Ref. [34]. The $\delta A_{ij}^{(st)}$ denotes the statistical error and the $\delta A_{ij}^{(sy)}$ denotes the systematic one.

$\theta_{c.m.}$	A_y^d	$\delta A_y^{d(st)}$	$\delta A_y^{d(sy)}$	A_{yy}	$\delta A_{yy}^{(st)}$	$\delta A_{yy}^{(sy)}$	A_{xx}	$\delta A_{xx}^{(st)}$	$\delta A_{xx}^{(sy)}$	A_{xz}	$\delta A_{xz}^{(st)}$	$\delta A_{xz}^{(sy)}$
82.0	−0.309	0.001	0.008	0.246	0.001	0.006	−0.225	0.001	0.006	0.253	0.013	0.029
88.0	−0.403	0.001	0.010	0.312	0.001	0.008	−0.207	0.001	0.005	0.320	0.014	0.037
94.0	−0.477	0.001	0.012	0.383	0.001	0.009	−0.168	0.001	0.004	0.377	0.015	0.044
100.0	−0.514	0.001	0.013	0.452	0.001	0.011	−0.111	0.001	0.003	0.407	0.017	0.047
110.0	−0.488	0.002	0.012	0.542	0.002	0.013	−0.001	0.002	0.001	0.366	0.026	0.043
119.1	−0.383	0.002	0.011	0.578	0.002	0.017	0.067	0.002	0.004	0.213	0.028	0.047

^{12}C(d,α)^{10}B*[2$^+$] at 0° [34]. Tables II and III show the data. The previously reported data in Ref. [21] were not extracted with these new calibration data but with those obtained using the ^{12}C($\vec{d},p$)^{13}C reaction or ^{3}He($\vec{d},p$)^{4}He reaction at low energies [20,41]. In the analysis in Ref. [21], the analyzing power data at $\theta_{c.m.}=90.0°$ and 110.0° were used to determine the beam polarizations for 135 and 70 MeV/nucleon, respectively. In Figs. 8 and 9, the new calibration data of Ref. [34] are compared with the data of Refs. [20,21]. Only the statistical errors are shown. These independent measurements, which used different methods to determine the beam polarizations, provide a reasonably good agreement at 135 MeV/nucleon. However, there are systematic discrepancies at 70 MeV/nucleon. This disagreement is due to the systematic uncertainties associated with the determination of the polarization axis (less than 5%) and the uncertainties in the magnitudes of the beam polarizations (less than 4%). The re-analyzed data at 70 MeV/nucleon, which were obtained using the new calibration data are tabulated in Tables IV and V and are shown in Fig. 10 with their statistical errors. The open diamonds (open triangles) in Fig. 10 are the results measured with the SMART system (D-room polarimeter). The newly analyzed data are in reasonable agreement with the calibration data of Ref. [34]. It should be noted that the A_{yy} at $\theta_{c.m.}=116.9°$ of 135 MeV/nucleon was reanalyzed in a similar way using deuteron beam polarizations measured at $\theta_{c.m.}=86.5°$ for d-p elastic scattering. These new polarizations reduced A_{yy} at $\theta_{c.m.}=116.9°$, which is shown with an open square in Fig. 8, by about 9%.

IV. THEORETICAL FORMALISM AND DYNAMICAL INPUT

In this paper we study elastic Nd scattering with the initial state ϕ composed of a deuteron and a nucleon. The outgoing state ϕ' corresponds to a change of the outgoing nucleon momentum. Using the matrix element of the elastic scattering transition operator U which is defined as

$$\langle\phi'|U|\phi\rangle = \langle\phi'|PG_0^{-1} + V_4^{(1)}(1+P) + PT$$
$$+ V_4^{(1)}(1+P)G_0\,T|\phi\rangle, \qquad (27)$$

the various spin observables and differential cross section can be calculated [36,42]. The quantity G_0 is the free $3N$ propagator and P takes into account the identity of nucleons and is the sum of a cyclical and an anticyclical permutation of three nucleons. $V_4^{(1)}$ represents one of the terms of the $3N$ force V_4,

$$V_4 = V_4^{(1)} + V_4^{(2)} + V_4^{(3)}, \qquad (28)$$

where each $V_4^{(i)}$ is symmetric under the exchange of the nucleons jk with $j \neq i \neq k$. In the 2π-exchange 3NF, $V_4^{(1)}$ is a contribution to the $3N$ potential from (off-shell) rescattering of a pion on nucleon 1. The first term in Eq. (27) is a single nucleon exchange contribution and is followed by a single interaction of three nucleons via the 3NF. The remaining part results from rescattering among three nucleons induced by two- and three-nucleon forces. All these rescatterings are summed up in the integral equation for the amplitude T [42,43],

$$T = tP\phi + (1+tG_0)V_4^{(1)}(1+P)\phi + tPG_0T$$
$$+ (1+tG_0)V_4^{(1)}(1+P)G_0T, \qquad (29)$$

where the NN t-operator is denoted by t. After projecting on a partial-wave momentum-space basis this equation leads to a system of coupled integral equations which can be solved numerically exactly for any nuclear force. In this study we

TABLE III. Calibrated analyzing power data for d-p elastic scattering at 135 MeV/nucleon reported in Ref. [34]. For the descriptions of the $\delta A_{ij}^{(st)}$ and $\delta A_{ij}^{(sy)}$, see Table I.

$\theta_{c.m.}$	A_y^d	$\delta A_y^{d(st)}$	$\delta A_y^{d(sy)}$	A_{yy}	$\delta A_{yy}^{(st)}$	$\delta A_{yy}^{(sy)}$	A_{xx}	$\delta A_{xx}^{(st)}$	$\delta A_{xx}^{(sy)}$	A_{xz}	$\delta A_{xz}^{(st)}$	$\delta A_{xz}^{(sy)}$
80.6	−0.345	0.001	0.011	0.398	0.001	0.012	−0.494	0.001	0.015	0.405	0.005	0.036
83.6	−0.374	0.001	0.011	0.424	0.001	0.013	−0.481	0.001	0.014	0.433	0.005	0.039
86.6	−0.393	0.001	0.012	0.446	0.001	0.013	−0.471	0.001	0.014	0.449	0.005	0.040
89.6	−0.413	0.001	0.013	0.469	0.001	0.014	−0.457	0.001	0.014	0.454	0.005	0.041
92.6	−0.420	0.001	0.013	0.498	0.001	0.015	−0.442	0.001	0.013	0.460	0.006	0.041
117.7	−0.346	0.002	0.012	0.628	0.002	0.018	−0.327	0.002	0.010	0.478	0.008	0.043
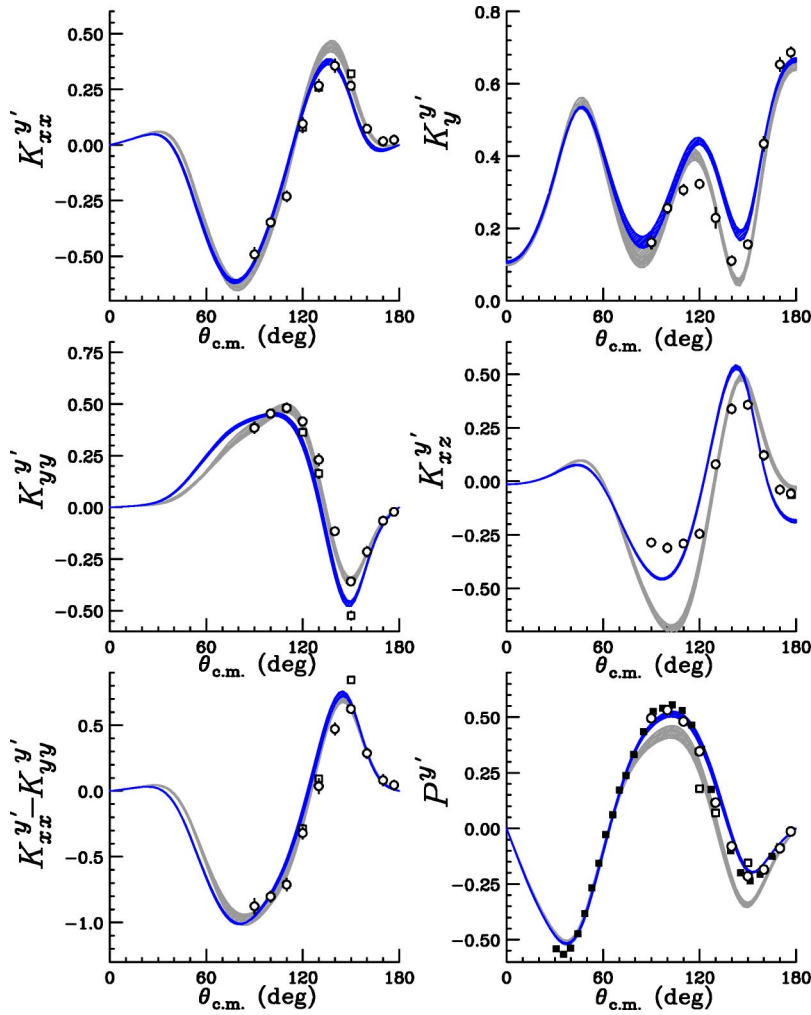
FIG. 7. (Color online) polarization-transfer coefficients $K_{xx}^{y'}$, $K_{yy}^{y'}$, $K_{xx}^{y'}-K_{yy}^{y'}$, $K_{y}^{y'}$, $K_{xz}^{y'}$, and the induced polarization $P^{y'}$ in elastic d-p scattering at 135 MeV/nucleon. The light shaded bands contain the combinations of the NN + TM force predictions while the dark shaded bands include the combinations with TM′(99). For the descriptions of symbols, see Fig. 6.
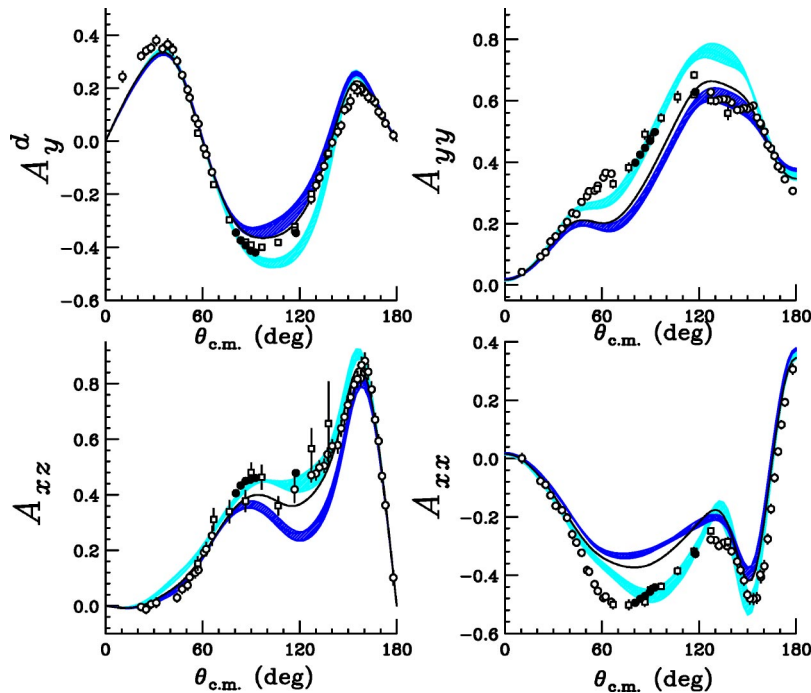

FIG. 8. (Color online) vector and tensor deuteron analyzing powers for d-p elastic scattering at 135 MeV/nucleon reported in [21,34]. Solid circles are the new calibration data of [34] while open squares and circles are the results presented in [21]. For the descriptions of bands and curves, see Fig. 6.
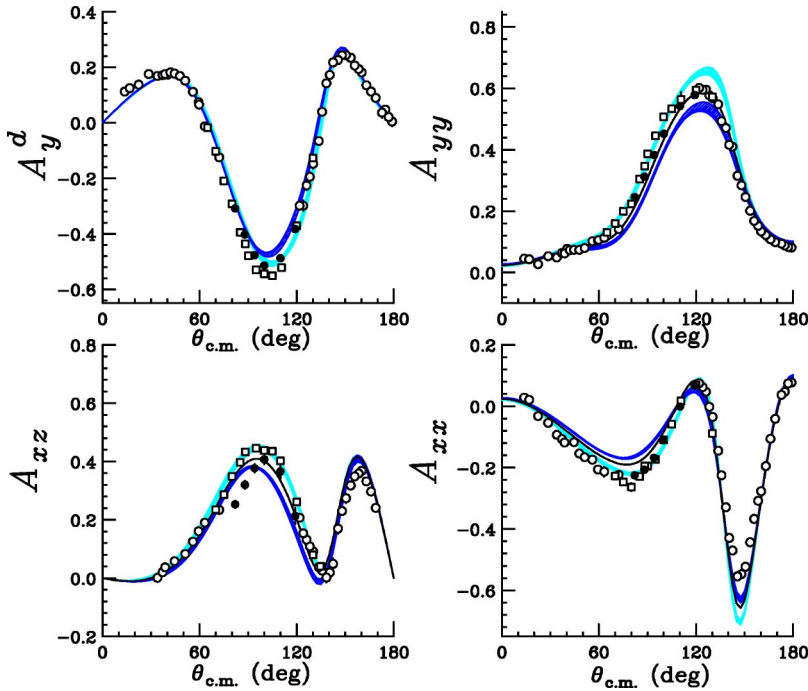
FIG. 9. (Color online) deuteron analyzing powers at 70 MeV/nucleon. For descriptions of symbols, see Fig. 8.

restricted our partial-wave basis taking all states with the total angular momenta j in the two-nucleon subsystem smaller than 6. This corresponds to a maximal number of 142 partial-wave states in the 3N system for each total angular momentum. For the energies of the present paper this provides convergent results for the elastic scattering observables. We checked that the convergence has been achieved by looking at the results obtained when $j=6$ states have been included. This increases the number of states to 194. This convergence check was done without 3NF. The inclusion of the 3NF has been carried through for all total angular momenta of the 3N system up to $J=13/2$ while the longer ranged 2N interactions require states up to $J=25/2$. For the details of the formalism and the numerical performance we refer to Refs. [42,44,45].

In this study predictions of different nuclear force models are shown. They consist of one of the NN forces: AV18, CDBonn, Nijmegen I, II and 93, and a 3NF. Each of the NN interactions was combined with the 2π-exchange TM 3NF model [10]. The combinations use the cut-off parameter Λ in the strong form factor parametrization separately adjusted to the ^{3}H binding energy for the different NN forces [46]. The Λ-values used with the AV18, CDBonn, Nijmegen I, II, and 93 potentials are $\Lambda=5.215$, 4.856, 5.120, 5.072, and 5.212 (in units of m_π), respectively. The standard parametrization of the TM 3NF was criticized in Refs. [12,13,47] since it violates chiral symmetry. A form more consistent with chiral symmetry was proposed by modifying the c-term of the TM force and absorbing the long range part of this term into the a-term and rejecting the rest of the c-term [12,13]. This new

TABLE IV. Data table for analyzing powers for d-p elastic scattering at 70 MeV/nucleon measured with the D-room polarimeter.

$\theta_{\text{c.m.}}$ (deg)	A_y^d	δA_y^d	A_{yy}	δA_{yy}	A_{xx}	δA_{xx}	A_{xz}	δA_{xz}
65.0	−0.016	0.002	0.121	0.004				
70.1	−0.097	0.003	0.148	0.006	−0.216	0.005	0.207	0.006
75.0	−0.190	0.004	0.186	0.007	−0.241	0.005	0.266	0.005
80.0	−0.276	0.007	0.228	0.014	−0.244	0.011	0.299	0.008
85.0	−0.369	0.004	0.280	0.004	−0.224	0.006	0.350	0.006
88.2	−0.405	0.004	0.328	0.004	−0.212	0.007	0.378	0.006
90.0	−0.448	0.004	0.355	0.004	−0.208	0.006		
95.0	−0.501	0.005	0.403	0.009	−0.166	0.006	0.395	0.006
100.0	−0.511	0.004	0.450	0.008	−0.095	0.005	0.388	0.008
105.0	−0.521	0.005	0.499	0.004	−0.063	0.006	0.385	0.008
110.0	−0.493	0.007	0.536	0.008	0.015	0.005	0.368	0.012
120.0	−0.352	0.006	0.577	0.012	0.060	0.007	0.220	0.010
130.0	−0.120	0.008	0.557	0.007	−0.074	0.015	0.094	0.012

TABLE V. Data table for analyzing powers for *d-p* elastic scattering at 70 MeV/nucleon measured with the SMART system.

$\theta_{\text{c.m.}}$ (deg)	A_y^d	δA_y^d	A_{yy}	δA_{yy}	A_{xx}	δA_{xx}	A_{xz}	δA_{xz}
13.7	0.113	0.004	0.036	0.005	0.039	0.004		
16.8	0.121	0.004	0.037	0.005	0.016	0.005		
22.4	0.129	0.005	0.043	0.006	−0.033	0.005		
28.6	0.163	0.005	0.055	0.006	−0.056	0.005		
33.9	0.162	0.004	0.059	0.006	−0.088	0.005	0.006	0.005
37.1	0.171	0.005	0.068	0.006	−0.103	0.005	0.008	0.006
38.7	0.175	0.005	0.066	0.006	−0.114	0.006	0.018	0.006
40.3	0.169	0.005	0.070	0.007				
41.9	0.173	0.006	0.071	0.007				
44.5	0.165	0.003	0.077	0.004	−0.111	0.005	0.029	0.007
47.8	0.155	0.004	0.078	0.004	−0.150	0.006		
51.2	0.135	0.004	0.089	0.004	−0.167	0.009	0.061	0.007
55.9	0.110	0.004	0.108	0.004	−0.172	0.006	0.111	0.006
59.4	0.072	0.004	0.112	0.004	−0.204	0.005	0.134	0.005
59.7	0.068	0.006	0.108	0.006				
63.3	−0.001	0.006	0.106	0.006	−0.214	0.008	0.160	0.011
72.1	−0.134	0.005	0.163	0.005	−0.221	0.009	0.216	0.013
121.8	−0.337	0.006	0.579	0.003	0.077	0.006	0.196	0.011
124.1	−0.330	0.011	0.578	0.006	0.063	0.008	0.144	0.008
126.1	−0.271	0.011	0.574	0.005	0.048	0.008	0.112	0.013
128.2	−0.192	0.011	0.572	0.008	−0.003	0.008	0.093	0.012
130.2	−0.150	0.011	0.559	0.008	−0.035	0.008	0.081	0.012
133.7	−0.040	0.007	0.547	0.006	−0.138	0.006	0.037	0.005
135.7	0.009	0.007	0.479	0.006	−0.215	0.006	0.026	0.007
138.4	0.097	0.006	0.448	0.005	−0.334	0.011	0.026	0.006
140.4	0.161	0.006	0.425	0.005	−0.434	0.010	0.058	0.007
142.5	0.181	0.005	0.397	0.005	−0.476	0.010	0.079	0.007
145.6	0.223	0.006	0.322	0.006	−0.558	0.008	0.198	0.007
148.0	0.227	0.005	0.279	0.005	−0.552	0.007	0.255	0.006
150.5	0.234	0.005	0.248	0.005	−0.528	0.007	0.302	0.006
153.4	0.219	0.006	0.198	0.007	−0.456	0.009	0.343	0.006
155.9	0.203	0.006	0.176	0.006	−0.370	0.008	0.367	0.005
158.3	0.171	0.005	0.137	0.006	−0.310	0.007	0.372	0.005
160.2	0.166	0.007	0.129	0.009	−0.279	0.008	0.365	0.008
163.1	0.127	0.006	0.122	0.008	−0.192	0.006	0.329	0.007
166.0	0.106	0.005	0.110	0.007	−0.100	0.005	0.284	0.006
168.8	0.078	0.005	0.101	0.007	−0.032	0.005	0.226	0.006
172.8	0.023	0.012	0.103	0.013	0.046	0.005		
174.8	0.020	0.009	0.090	0.011	0.052	0.004		
176.9	0.015	0.008	0.088	0.010	0.077	0.004		
179.0	0.002	0.011	0.085	0.012	0.087	0.005		

form is called TM′(99) [14]. The Λ-values used (again in units of m_π) with the AV18, CDBonn, Nijmegen I, and II potentials are $\Lambda=4.764$, 4.469, 4.690, and 4.704, respectively.

For the AV18 potential we also use the Urbana IX 3NF [11]. That force is based on the Fujita-Miyazawa assumption

of an intermediate Δ excitation in the 2π exchange [9], which is augmented by a phenomenological spin-independent short-range part. This force is formulated in configuration space [11]. Refer to Ref. [28] for the partial-wave decomposition of the Urbana IX 3NF in momentum space.
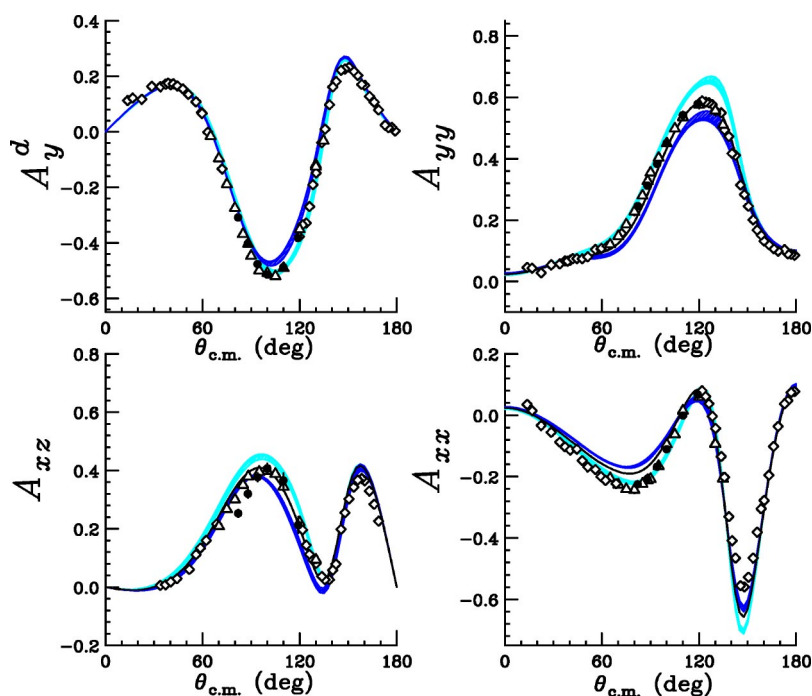
FIG. 10. (Color online) deuteron analyzing powers at 70 MeV/nucleon obtained using the new calibration data. Open diamonds are the results measured with the SMART system and open triangles show the results measured with the D-room polarimeter. For the descriptions of bands and curves, see Fig. 6.

V. DISCUSSION

A. Comparison of present data with theoretical predictions

In Figs. 6 and 7 the theoretical predictions for the five different NN potentials and their combinations with 3NF's are shown for the polarization-transfer coefficients and the induced polarization. The light shaded bands in Fig. 6 are the results of the Faddeev calculations based on the high-precision NN potentials, AV18, CDBonn, Nijmegen I, II and 93 only. The dark shaded bands in Fig. 6 contain the predictions of the four NN forces with the TM′(99) 3NF. In each case the triton binding energy was adjusted to the experimental value. The solid curves in Fig. 6 are the theoretical predictions obtained using the AV18 potential combined with the Urbana IX 3NF. To avoid making the figure too complicated the predictions combining the five NN forces with the TM 3NF are shown in Fig. 7 together with the calculations of TM′(99) 3NF. The TM 3NF predictions are shown as light shaded bands and the TM′(99) 3NF ones are shown as dark shaded bands in that figure.

At first, theoretical predictions are separately compared to the data for the polarization-transfer coefficients $K_{xx}^{y'}$ and $K_{yy}^{y'}$. For $K_{xx}^{y'}$, the 3NF effects are rather modest and the differences among the various 3NFs are small. However, the data apparently prefer the 3NF predictions rather than the pure $2N$ force ones. The deviation of the 3NF predictions from those for the $2N$ forces is clearly pronounced for $K_{yy}^{y'}$, and the $2N$ band significantly overestimates the data at the angles $\theta_{\text{c.m.}}=90°-120°$. The inclusion of the Urbana IX 3NF provides a good description of the data. Also the TM′(99) does fairly well, whereas the TM provides a better description of the data. One can see clearly the difference between the data and the $2N$ force predictions for the polarization-transfer coefficient $K_{xx}^{y'}-K_{yy}^{y'}$. The $2N$ force predictions underestimate the

data in the region of the $K_{xx}^{y'}-K_{yy}^{y'}$ minima at the angles $\theta_{\text{c.m.}}=90°-120°$. The inclusion of the Urbana IX 3NF as well as TM′(99) removes these discrepancies. Also for the TM 3NF there is a good agreement between the data and theory. For $K_{y}^{y'}$ at backward angles $\theta_{\text{c.m.}}\geqslant150°$ the data support the NN forces only predictions as well as the TM′(99) and Urbana IX 3NFs ones. In the angular range of $\theta_{\text{c.m.}}=90°-120°$, a large discrepancy exists between the $2N$ force only predictions and the data. The inclusion of either TM′(99) or Urbana IX 3NF shifts the calculated results in the right direction, but not enough to describe the data. The effects of the TM 3NF are also not sufficient to provide a good description of the data. For $K_{xz}^{y'}$ the situation is complicated throughout the entire measured angular range and the data are not described by the theoretical predictions. At backward angles $\theta_{\text{c.m.}}\geqslant150°$, the $2N$ band provides a moderate agreement with the data. It clearly deviates from the data in the minimum region around $\theta_{\text{c.m.}}=100°$, but the predictions with 3NFs included do not explain this discrepancy. It is interesting to note that all 3NF models studied predict large effects in the region of this minimum, however the effects of the TM′(99) and Urbana IX 3NFs are in opposite directions to those of the TM 3NF. For the induced polarization $P^{y'}$ the $2N$ band overestimates the data around the region of the $P^{y'}$ maximum. The inclusion of the Urbana IX or TM′(99) 3NF brings the predictions closer to the data, while the TM 3NF provides large, incorrect effects. For the analyzing powers in p-d elastic scattering at incoming nucleon energies larger than about 60 MeV, a similar pattern of discrepancies between data and theoretical predictions is found [27,28].

The predictions including the TM′(99) 3NF, which were not presented in our previous study [21], are compared with our deuteron analyzing powers at 135 and 70 MeV/nucleon in Figs. 8 and 10, respectively. A comparison of the vector and tensor analyzing powers to the TM′(99) predictions

shown in Figs. 8 and 10 reveals that the effects of the TM′(99) 3NF are similar in size and directions to the effects of the Urbana IX 3NF, except for A_{xz} at 135 MeV/nucleon.

B. Summary of the comparison between *d-p* polarization data and theoretical predictions

In this section we would like to summarize the comparison of the theoretical predictions to *d-p* elastic scattering data reported here and in Ref. [21]. It encompasses all deuteron analyzing powers A_y^d, A_{xx}, A_{yy}, A_{xz}, the proton induced polarization $P^{y'}(=-A_y^p)$, and the deuteron-to-proton polarization-transfer coefficients $K_y^{y'}$, $K_{xx}^{y'}-K_{yy}^{y'}$ ($K_{xx}^{y'}$, $K_{yy}^{y'}$), and $K_{xz}^{y'}$.

Generally, the discrepancies between the data and the pure 2*N* force predictions are clearly seen at the angles where the cross sections have minima. For the cross sections these discrepancies at the two energies considered here are explained by taking into account the 2π-exchange type 3NF models [TM, TM′(99), and Urbana IX]. Thus all 2π-exchange 3NF potentials considered here [TM, TM′(99), and Urbana IX] provide 3NF effects for the cross sections which are comparable in magnitude and sign. At higher energies, however, discrepancies remain in the minima and even more at backward angles, Refs. [19,48].

Spin observables can be grouped into three types. The **Type I** observables are the deuteron vector analyzing power A_y^d and the deuteron-to-proton polarization-transfer coefficient $K_{xx}^{y'}-K_{yy}^{y'}$ ($K_{xx}^{y'}$, $K_{yy}^{y'}$). The deviations between the data and the 2*N* force predictions for these observables are explained by the inclusion of the 2π-exchange 3NFs considered here [TM, TM′(99), Urbana IX] similarly as in the case of the cross section. These observables provide clear evidence for 3NFs.

The **Type II** observable is the proton induced polarization $P^{y'}$, which is equivalent to the proton analyzing power $A_y^p(P^{y'}=-A_y^p)$. The TM′(99) 3NF and Urbana IX 3NF describe the difference between the data and the 2*N* force predictions. The inclusion of the TM 3NF shifts the calculated results in the right direction, but the effects are too large. The nonzero *c*-term of the TM 3NF might be the origin of the incorrect 3NF effect. In order to see this more clearly, it is interesting to identify the effects due to the intermediate Δ-isobar excitation which is the main part of the 2π-exchange 3NF. Recently, the Hannover group carried out calculations which explicitly included the Δ-isobar excitation in the framework of the coupled-channel approach [49]. In their calculations, the CDBonn potential was taken as the 2*N* interaction. One can get directly the Δ-isobar effects (magnitude and/or direction) by comparing their predictions with and without the Δ-isobar excitation. The results are shown in Figs. 11 and 12. The Δ-isobar effects are similar to those of the TM′(99) and Urbana IX 3NFs for almost all observables except for A_{xx}. This feature indicates that the poor agreement for TM in $P^{y'}$ of **Type II** is not due to the 2π-exchange Δ-isobar excitation. Since the main difference between the TM and TM′(99) 3NFs comes from the nonvanishing *c*-term

in the TM 3NF, this term is most probably responsible for the poor description of $P^{y'}$ by the TM 3NF.

The **Type III** observables are the deuteron tensor analyzing powers A_{xx}, A_{yy}, A_{xz}, and the deuteron-to-proton polarization transfer coefficients $K_y^{y'}$, and $K_{xz}^{y'}$. No calculation shows a superiority for these observables. Although large effects of 3NFs are predicted at the angles $\theta_{c.m.}=90°-120°$, they are not supported by the data. It is interesting to note that the TM′(99) and Urbana IX 3NFs provide very similar effects. On the other hand, the effects induced by the TM 3NF are quite different from the TM′(99) and Urbana IX 3NF's ones. The **Type III** observables clearly reveal the defects of the present day 3NF models. To describe these spin observables one should look for other 3NF terms in addition to the 2π-exchange 3NFs. At low energies, Witała *et al.* applied 3NFs based on π-ρ and ρ-ρ exchanges [50,51] and investigated their effects on cross sections and spin observables for *Nd* elastic scattering [52]. It was found that the effects of the π-ρ exchange generally reduced the effects caused by the 2π-exchange TM 3NF. The effects induced by ρ-ρ exchanges were negligible. It would be interesting to apply these π-ρ and ρ-ρ exchange 3NFs also at intermediate energies where the interferences might be different. Recently, new 3NF models called the Illinois models have been reported [15] and found to be successful in describing the binding and excitation energies of light nuclei with mass number up to $A=10$. The models are an extension of the Urbana IX 3NF and consist of five terms: the two-pion-exchange terms due to πN scattering in *S* and *P* waves, a phenomenological repulsive term, and the three-pion-exchange terms ($V^{3\pi,\Delta R}$) due to ring diagrams with Δ in the intermediate states. The $V^{3\pi,\Delta R}$ is a new type of 3NF and contains new spin dependent terms, such as $\vec{\sigma}\cdot(\vec{r}_{ij}\times\vec{r}_{jk})$ term. These spin dependent terms might explain **Type III** spin observables. It would be interesting to include these new terms into the 3*N* continuum calculations. The results of the coupled-channel formulations with the Δ-isobar excitations are supported by the tensor analyzing power A_{xx} [49] data, which are not well described by the TM′(99) as well as Urbana IX 3NFs. This points to contributions which are not included in 2π-exchange 3NF models.

As the incident nucleon energy increases one should not ignore relativity which becomes more and more important. Some indications on its importance was found in the analysis of the high-precision *nd* total cross section data [53] and in the study of backward angles of *p-d* elastic scattering cross section data at higher energies [19,48]. The discrepancies between the data and nonrelativistic predictions become larger with increasing energy and cannot be removed by including different 3NFs [53]. Therefore, relativity might be another candidate to provide a solution for the **Type III** spin observables. Work along this line is in progress [54,55].

In chiral-perturbation theory at NNLO [56] the 2π-exchange 3NF together with a one-pion exchange between a *NN* contact force and the third nucleon, and a pure 3*N* contact force occurs. This also suggests that the 2π-exchange should be supplemented by the exchange of a pion together with heavy mesons and the exchange of two heavy mesons. In addition quite a few types of 3NFs appear
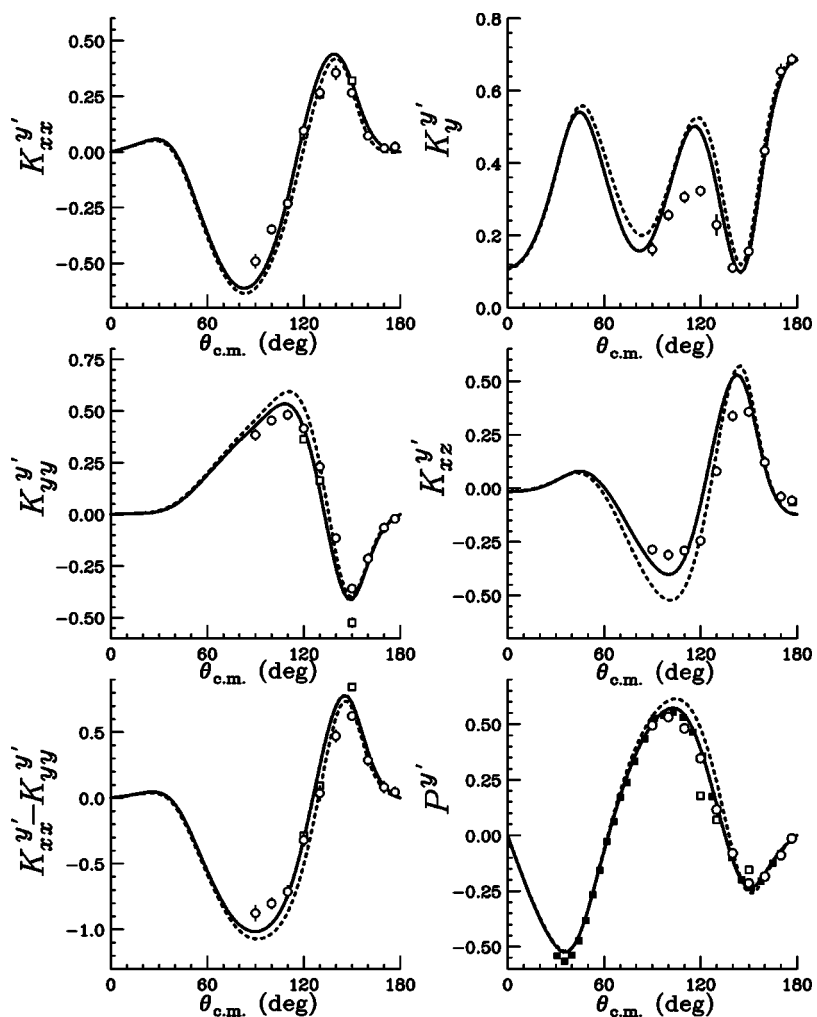
POLARIZATION TRANSFER MEASUREMENT FOR ^{1}H($\vec{d},\vec{p}$)^{2}H...

PHYSICAL REVIEW C **70**, 014001 (2004)

FIG. 11. Polarization-transfer coefficients $K_{xx}^{y'}$, $K_{yy}^{y'}$, $K_{xx}^{y'}-K_{yy}^{y'}$, $K_{y}^{y'}$, $K_{xz}^{y'}$, and the induced polarization $P^{y'}$ in elastic d-p scattering at 135 MeV/nucleon. The solid curves are the coupled-channel approach predictions obtained with Δ-isobar excitations and the dotted curves are based on the CDBonn potential (Ref. [49]). For the descriptions of symbols, see Fig. 6.
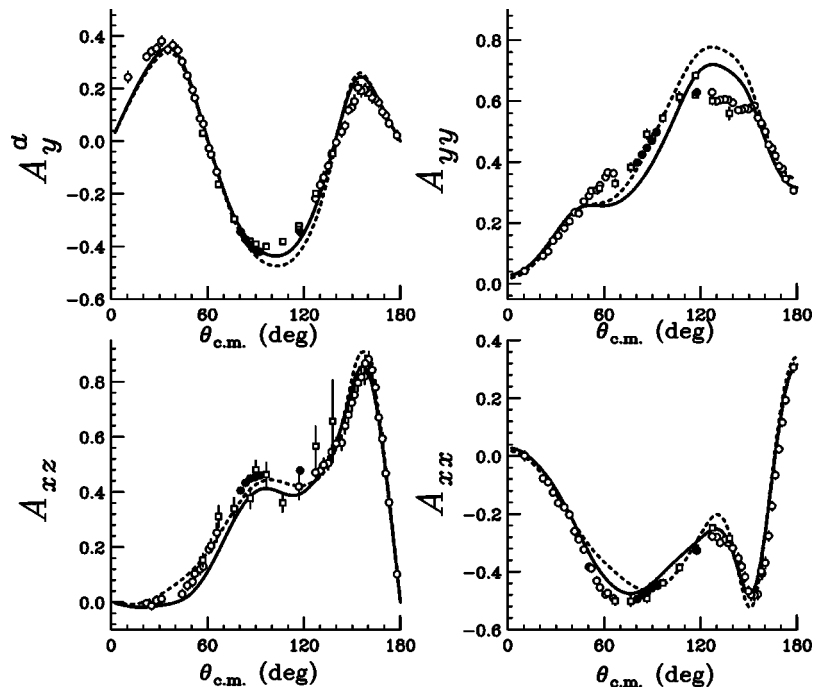
FIG. 12. Vector and tensor deuteron analyzing powers in elastic d-p scattering at 135 MeV/nucleon. For the descriptions of curves see Fig. 11. For the descriptions of symbols, see Fig. 8.

at NNNLO, which have to be worked out. This will lead to additional spin-dependences, which will be required for the **Type III** observables.

VI. SUMMARY AND CONCLUSION

The deuteron-to-proton $(\vec{d}+p \rightarrow \vec{p}+d)$ polarization-transfer coefficients $K_y^{y'}$, $K_{xx}^{y'}-K_{yy}^{y'}$ ($K_{xx}^{y'}$, $K_{yy}^{y'}$), and $K_{xz}^{y'}$ were measured at 135 MeV/nucleon in the angular range $\theta_{\text{c.m.}} = 90° - 180°$. The induced proton polarization $P^{y'}$ was also measured. The statistical uncertainties are smaller than 0.03 for all the polarization-transfer coefficients, and 0.02 for the induced polarization $P^{y'}$. The estimated systematic uncertainties for the polarization-transfer coefficients and the induced polarization $P^{y'}$ are about 8%. The induced polarization $P^{y'}$ was compared with the analyzing power A_y^p for the time-reversed reaction, $^2\text{H}(\vec{p},p)^2\text{H}$ elastic scattering, measured at KVI. The data are consistent within the statistical uncertainties in the measured angular range.

In our previous study, the measurements of a complete set of deuteron analyzing powers were measured at incoming deuteron energies 70, 100, and 135 MeV/nucleon, covering a wide angular range $\theta_{\text{c.m.}} = 10° - 180°$. Also the unpolarized cross sections were measured at the same angles at 70 and 135 MeV/nucleon. High-precision data have been obtained.

Our data are compared with predictions based on different modern nuclear forces in order to look for evidence of 3NF effects and to test present-day 3NF models. Based on the comparison of our data with pure $2N$ force predictions clear discrepancies, which increase with deuteron energy, are found for most observables, especially at the angles around the cross-section minimum. Including any of the 2π-exchange 3NFs used in the present paper, the TM 3NF, the modified version of it TM′(99), and the Urbana IX 3NF, can reduce the discrepancies observed for the cross section, for the deuteron vector analyzing power A_y^d, and for the polarization-transfer coefficient $K_{xx}^{y'}-K_{yy}^{y'}$ ($K_{xx}^{y'}$, $K_{yy}^{y'}$). Thus, these observables can be considered to provide a clear evidence for the 3NF effects. For the induced polarization $P^{y'}$, the TM′(99) and Urbana IX 3NFs explain the difference between the data and the $2N$ force predictions. On the other hand, the TM 3NF fails to describe this observable. This appears to indicate that the nonvanishing c-term of the TM 3NF, which should not exist according to chiral symmetry, is probably responsible for the failure of the model. For the tensor analyzing powers and the polarization-transfer coefficients $K_y^{y'}$ and $K_{xz}^{y'}$, calculations fail to describe the data. Large effects of 3NFs are predicted at the angles $\theta_{\text{c.m.}} = 90° - 120°$. However, the data do not support these predictions. Our results clearly reveal the defects of the present day 3NFs.

Finally, it should be noted that this is the first precise data set for the analyzing powers, and polarization-transfer coefficients for d-p elastic scattering at intermediate energies, which will provide a solid basis to test future 3NF models.

[1] R. B. Wiringa, V. G. J. Stoks, and R. Schiavilla, Phys. Rev. C **51**, 38 (1995).

[2] R. Machleidt, K. Holinde, and Ch. Elster, Phys. Rep. **149**, 1 (1987).

[3] R. Machleidt, Adv. Nucl. Phys. **19**, 189 (1989).

[4] R. Machleidt, Phys. Rev. C **63**, 024001 (2001).

[5] V. G. J. Stoks, R. A. M. Klomp, C. P. F. Terheggen, and J. J. de Swart, Phys. Rev. C **49**, 2950 (1994).

[6] A. Nogga, H. Kamada, and W. Glöckle, Phys. Rev. Lett. **85**, 944 (2000); A. Nogga, H. Kamada, W. Glöckle, and B. R. Barrett, Phys. Rev. C **65**, 054003 (2002).

[7] J. Carlson and R. Schiavilla, Rev. Mod. Phys. **70**, 743 (1998).

[8] R. B. Wiringa, S. C. Pieper, J. Carlson, and V. R. Pandharipande, Phys. Rev. C **62**, 014001 (2000); S. C. Pieper, K. Varga, and R. B. Wiringa, *ibid.* **66**, 044310 (2002).

[9] J. Fujita and H. Miyazawa, Prog. Theor. Phys. **17**, 360 (1957).

[10] S. A. Coon, M. D. Schadron, P. C. McNamee, B. R. Barrett, D. W. E. Blatt, and B. H. J. McKellar, Nucl. Phys. **A317**, 242 (1979); S. A. Coon and W. Glöckle, Phys. Rev. C **23**, 1790 (1981); S. A. Coon, Few-Body Syst., Suppl. **1**, 41 (1984); S. A. Coon and J. L. Friar, Phys. Rev. C **34**, 1060 (1986).

[11] B. S. Pudliner, V. R. Pandharipande, J. Carlson, S. C. Pieper, and R. B. Wiringa, Phys. Rev. C **56**, 1720 (1997).

[12] J. L. Friar, D. Hüber, and U. van Kolck, Phys. Rev. C **59**, 53 (1999).

[13] D. Hüber, J. L. Friar, A. Nogga, H. Witała, and U. van Kolck, Few-Body Syst. **30**, 95 (2001).

[14] S. A. Coon and H. K. Han, Few-Body Syst. **30**, 131 (2001).

[15] S. C. Pieper, V. R. Pandharipande, R. B. Wiringa, and J. Carlson, Phys. Rev. C **64**, 014001 (2001).

[16] H. Witała, W. Glöckle, D. Hüber, J. Golak, and H. Kamada, Phys. Rev. Lett. **81**, 1183 (1998).

[17] S. Nemoto, K. Chmielewski, S. Oryu, and P. U. Sauer, Phys. Rev. C **58**, 2599 (1998).

[18] H. Sakai, K. Sekiguchi, H. Witała, W. Glöckle, M. Hatano, H. Kamada, H. Kato, Y. Maeda, A. Nogga, T. Ohnishi, H. Oka-

mura, N. Sakamoto, S. Sakoda, Y. Satou, K. Suda, A. Tamii, T. Uesaka, T. Wakasa, and K. Yako, Phys. Rev. Lett. **84**, 5288 (2000).

[19] K. Hatanaka, Y. Shimizu, D. Hirooka, J. Kamiya, Y. Kitamura, Y. Maeda, T. Noro, E. Obayashi, K. Sagara, T. Saito, H. Sakai, Y. Sakemi, K. Sekiguchi, A. Tamii, T. Wakasa, T. Yagita, K. Yako, H. P. Yoshida, V. P. Ladygin, H. Kamada, W. Glöckle, J. Golak, A. Nogga, and H. Witała, Phys. Rev. C **66**, 044002 (2002).

[20] N. Sakamoto, H. Okamura, T. Uesaka, S. Ishida, H. Otsu, T. Wakasa, Y. Satou, T. Niizeki, K. Katoh, T. Yamashita, K. Hatanaka, Y. Koike, and H. Sakai, Phys. Lett. B **367**, 60 (1996).

[21] K. Sekiguchi, H. Sakai, H. Witała, W. Glöckle, J. Golak, M. Hatano, H. Kamada, H. Kato, Y. Maeda, J. Nishikawa, A. Nogga, T. Ohnishi, H. Okamura, N. Sakamoto, S. Sakoda, Y. Satou, K. Suda, A. Tamii, T. Uesaka, T. Wakasa, and K. Yako, Phys. Rev. C **65**, 034003 (2002).

[22] H. Kamada, D. Hüber, and A. Nogga, Few-Body Syst. **30**, 121 (2001).

[23] A. Kievsky, Phys. Rev. C **60**, 034001 (1999).

[24] R. V. Cadman, J. Brack, W. J. Cummings, J. A. Fedchak, B. D. Fox, H. Gao, W. Glöckle, J. Golak, C. Grosshauser, R. J. Holt, C. E. Jones, H. Kamada, E. R. Kinney, M. A. Miller, W. Nagengast, A. Nogga, B. R. Owen, K. Rith, F. Schmidt, E. C. Schulte, J. Sowinski, F. Sperisen, E. L. Thorsland, R. Tobey, J. Wilbert, and H. Witała, Phys. Rev. Lett. **86**, 967 (2001).

[25] R. Bieber, W. Glöckle, J. Golak, M. N. Harakeh, D. Hüber, H. Huisman, N. Kalantar-Nayestanaki, H. Kamada, J. G. Messchendorp, A. Nogga, H. Sakai, N. Sakamoto, M. Seip, M. Volkerts, S. Y. van der Werf, and H. Witała, Phys. Rev. Lett. **84**, 606 (2000).

[26] E. J. Stephenson, H. Witała, W. Glöckle, H. Kamada, and A. Nogga, Phys. Rev. C **60**, 061001 (1999).

[27] K. Ermisch, A. M. van den Berg, R. Bieber, W. Glöckle, J. Golak, M. Hagemann, V. M. Hannen, M. N. Harakeh, M. A. de Huu, N. Kalantar-Nayestanaki, H. Kamada, M. Kiš, J. Kuroś-Żołnierczuk, M. Mahjour-Shafiei, A. Micherdzińska, A. Nogga, R. Skibiński, H. Witała, and H. J. Wörtche, Phys. Rev. Lett. **86**, 5862 (2001).

[28] H. Witała, W. Glöckle, J. Golak, A. Nogga, H. Kamada, R. Skibiński, and J. Kuroś-Żołnierczuk, Phys. Rev. C **63**, 024007 (2001).

[29] T. Ichihara *et al.*, Nucl. Phys. **A569**, 287c (1994).

[30] S. Ishida *et al.*, High Energy Spin Physics, AIP Conf. Proc. No. 343 (AIP, New York, 1995), p. 182.

[31] H. Okamura *et al.*, Polarized Ion Sources and Polarized Gas Targets, AIP Conf. Proc. No. 293 (AIP, New York, 1994), p. 84.

[32] H. Okamura *et al.*, High Energy Spin Physics, AIP Conf. Proc. No. 343 (AIP, New York, 1995), p. 123.

[33] T. Uesaka *et al.*, RIKEN Accel. Prog. Rep. **35**, 148 (2002).

[34] K. Suda *et al.*, RIKEN Accel. Prog. Rep. **35**, 174 (2002).

[35] H. Okamura, Nucl. Instrum. Methods Phys. Res. A **443**, 194 (2000).

[36] G. G. Ohlsen, Rep. Prog. Phys. **35**, 717 (1972).

[37] H. O. Meyer, P. Schwandt, G. L. Moake, and P. P. Singh, Phys. Rev. C **23**, 616 (1981).

[38] H. O. Meyer, P. Schwandt, W. W. Jacobs, and J. R. Hall, Phys. Rev. C **27**, 459 (1983).

[39] M. W. McNaughton, B. E. Bonner, H. Ohnuma, O. B. van Dijk, Sun Tsu-Hsun, C. L. Hollas, D. J. Cremans, K. H. Mcnaughton, P. J. Riley, R. F. Rodebaugh, S. E. Turpin, B. Aas, and G. S. Weston, Nucl. Instrum. Methods Phys. Res. A **241**, 435 (1985).

[40] E. Aprile-Giboni, R. Hausammann, E. Heer, R. Hess, C. Lechanoine-Le Luc, W. Leo, S. Morenzoni, Y. Onel, and D. Rapin, Nucl. Instrum. Methods Phys. Res. **215**, 147 (1983).

[41] T. Uesaka *et al.*, RIKEN Accel. Prog. Rep. **33**, 153 (2000).

[42] W. Glöckle, H. Witała, D. Hüber, H. Kamada, and J. Golak, Phys. Rep. **274**, 107 (1996).

[43] D. Hüber, H. Kamada, H. Witała, and W. Glöckle, Acta Phys. Pol. B **28**, 1677 (1997).

[44] H. Witała, Th. Cornelius, and W. Glöckle, Few-Body Syst. **3**, 123 (1988).

[45] D. Hüber, H. Witała, and W. Glöckle, Few-Body Syst. **14**, 171 (1993).

[46] A. Nogga, D. Hüber, H. Kamada, and W. Glöckle, Phys. Lett. B **409**, 19 (1997).

[47] S. N. Yang, Phys. Rev. C **10**, 2067 (1974).

[48] K. Ermisch, H. R. Amir-Ahmadi, A. M. van den Berg, R. Castelijns, B. Davids, E. Epelbaum, E. van Garderen, W. Glöckle, J. Golak, M. N. Harakeh, M. Hunyadi, M. A. de Huu, N. Kalantar-Nayestanaki, H. Kamada, M. Kis, M. Mahjour-Shafiei, A. Nogga, R. Skibiński, H. Witała, and H. J. Wörtche, Phys. Rev. C **68**, 051001 (2003).

[49] A. Deltuva, R. Machleidt, and P. U. Sauer, Phys. Rev. C **68**, 024005 (2003).

[50] S. A. Coon and M. T. Peña, Phys. Rev. C **48**, 2559 (1993).

[51] S. A. Coon, M. T. Peña, and D. O. Riska, Phys. Rev. C **52**, 2925 (1995).

[52] H. Witała, D. Hüber, W. Glöckle, J. Golak, A. Stadler, and J. Adam, Jr., Phys. Rev. C **52**, 1254 (1995).

[53] H. Witała, H. Kamada, A. Nogga, W. Glöckle, Ch. Elster, and D. Hüber, Phys. Rev. C **59**, 3035 (1999).

[54] H. Kamada and W. Glöckle, Phys. Rev. Lett. **80**, 2547 (1998).

[55] H. Kamada, W. Glöckle, J. Golak, and Ch. Elster, Phys. Rev. C **66**, 044010 (2002).

[56] E. Epelbaum, A. Nogga, W. Glöckle, H. Kamada, Ulf-G. Meissner, and H. Witała, Phys. Rev. C **66**, 064001 (2002).